

Studies of regular and random magnetic fields in the ISM: statistics of polarization vectors and the Chandrasekhar-Fermi technique

Diego Falceta-Gonçalves¹

*Núcleo de Astrofísica Teórica, Universidade Cruzeiro do Sul - Rua Galvão Bueno 868,
CEP 01506-000 São Paulo, Brazil*

*Department of Astronomy, University of Wisconsin - 475 N. Charter Street, Madison WI
53706-1582, USA*

Alex Lazarian

*Department of Astronomy, University of Wisconsin - 475 N. Charter Street, Madison WI
53706-1582, USA*

and Grzegorz Kowal

*Department of Astronomy, University of Wisconsin - 475 N. Charter Street, Madison WI
53706-1582, USA*

Astronomical Observatory, Jagiellonian University, ul. Orła 171, 30-244 Kraków, Poland

ABSTRACT

Polarimetry is extensively used as a tool to trace the interstellar magnetic field projected on the plane of sky. Moreover, it is also possible to estimate the magnetic field intensity from polarimetric maps based on the Chandrasekhar-Fermi method. In this work, we present results for turbulent, isothermal, 3-D simulations of sub/supersonic and sub/super-Alfvénic cases. With the cubes, assuming perfect grain alignment, we created synthetic polarimetric maps for different orientations of the mean magnetic field with respect to the line of sight (LOS). We show that the dispersion of the polarization angle depends on the angle of the mean magnetic field regarding the LOS and on the Alfvénic Mach number. However, the second order structure function of the polarization angle follows the relation $SF \propto l^\alpha$, α being dependent exclusively on the Alfvénic Mach number.

¹email: diego.goncalves@unicsul.br; diego@astro.wisc.edu

The results show an anti-correlation between the polarization degree and the column density, with exponent $\gamma \sim -0.5$, in agreement with observations, which is explained by the increase in the dispersion of the polarization angle along the LOS within denser regions. However, this effect was observed exclusively on supersonic, but sub-Alfvénic, simulations. For the super-Alfvénic, and the subsonic model, the polarization degree showed to be independent on the column density. Our major quantitative result is a generalized equation for the CF method, which allowed us to determine the magnetic field strength from the polarization maps with errors $< 20\%$. We also account for the role of observational resolution on the CF method.

Subject headings: ISM: magnetic fields – techniques: polarimetric – methods: numerical, statistical

1. Introduction

It is believed that giant molecular clouds in the interstellar medium (ISM) are threaded by large scale magnetic fields (Schleuning 1998; Crutcher 1999). However, it is still not completely clear what is the role of the magnetic field in the dynamics of the ISM and what is its effect on the star formation process. Also, the ratio of the magnetic and turbulent energy in these environments is a subject of controversy (Padoan & Norlund 2002; Girart, Rao & Marrone 2006). Magnetic fields can influence the injection and evolution of turbulence bringing more complexity to this issue (see Lazarian & Cho [2004] for review). As an example, simulations have shown that strongly magnetized turbulent media develop structures with lower density contrasts when compared to pure hydrodynamic turbulence (Kowal, Lazarian & Beresniak 2007; Kritsuk et al. 2007).

Observationally, different techniques can be used to measure the ISM magnetic field and determine its intensity and topology. Zeeman splitting of spectral lines provides a direct and precise derivation of the magnetic field component along the line of sight (LOS), mainly for clouds presenting strong spectral lines (Heiles & Troland 2005). However, it cannot be applied to the clouds where the line intensities are too weak. Typically, when observed, Zeeman measurements of molecular clouds give $B_{\text{LOS}} \sim 10^{1-3} \mu\text{G}$, and suggest the correlation with density $B_{\text{LOS}} \propto \rho^{0.5}$, which is consistent to the expected relation for compressions of magnetic fields frozen into plasma. Spectral line broadening show that molecular clouds present supersonic, but critically Alfvénic motions (Crutcher et al. 1999). This fact shows that the turbulent motions may be excited by MHD modes instead of being purely hydrodynamical.

One of the most readily available methods of studying the perpendicular component of the magnetic field is based on the polarization of dust thermal emissions at infrared and submillimetric wavelengths (Hildebrand et al. 2000). The alignment of grains in respect to the magnetic field is a hot research topic (see Lazarian [2007] for review). Radiative torques (RATs) can promote alignment of irregular dust particles, resulting in different intensities for polarized radiation parallel and perpendicular to the local magnetic field (Dolginov & Mytrophanov 1996; Draine & Weingartner 1996, 1997; Lazarian & Hoang 2007a). Grains with long axis aligned perpendicular to the magnetic field induce polarization parallel to the magnetic field for transmitted star light, and perpendicular to the field lines for the dust emission. Cho & Lazarian (2005) showed that RATs are very efficient on the grain alignment process in molecular clouds, even for the very dense regions (up to $A_V < 10$). They also showed that the alignment efficiency strongly depends on the grain size, being practically perfect for large grains ($a > 0.1 \mu\text{m}$). More detailed studies of the RATs efficiency by Lazarian & Hoang (2007a) confirmed this claim. Therefore, for a range of A_V it is acceptable to assume that the grains are well-aligned.

For a given polarization map of an observed region, the mean polarization angle indicates the orientation of the large scale magnetic field. On the other hand the polarization dispersion gives clues on the value of the turbulent energy. This, as a consequence, can be used to determine the magnetic field component along the plane of sky. Chandrasekhar & Fermi (1953) introduced a method (CF method hereafter) for estimating the ISM magnetic fields based on the dispersions of the polarization angle and gas velocity. Simply, it is assumed that the magnetic field perturbations are Alfvénic and that the rms velocity is isotropic.

A promising approach to test this method is to create two-dimensional (plane of sky) synthetic maps from numerically simulated cubes. Ostriker, Stone & Gammie (2001) performed 3D-MHD simulations, with 256^3 resolution, in order to obtain polarization maps and study the validity of the CF method on the estimation of the magnetic field component along the plane of sky. They showed that the CF method gives reasonable results for highly magnetized media, in which the dispersion of the polarization angle is $< 25^\circ$. However, they did not present any other statistical analysis or predictions that could be useful for the determination of the ISM magnetic field from observations.

Heitsch et al. (2001) presented a complementary work, with a more detailed analysis regarding the limited observational resolution on the CF method, and presented a modified equation to account for the differences obtained previously. They concluded that lower observational resolution leads to an overestimation of the magnetic field from the CF equation. They also showed a good agreement between the CF technique and the expected magnetic field of their simulations, except for the weak field models.

Polarization maps from numerical simulations can also be used in the study of the correlation between the polarization degree and the total emission intensity (or dust column density). Observationally, the polarization degree in dense molecular clouds decreases with the total intensity as $P \propto I^{-\alpha}$, with $\alpha = 0.5 - 1.2$ (Gonçalves, Galli & Walmsley 2005). Padoan et al. (2001) studied the role of turbulent cells in the P versus I relation using supersonic and super-Alfvénic self-gravitating MHD simulations. They found a decrease of polarization degree with total dust emission within gravitational cores, in agreement with observations, if grains are assumed to be unaligned for $A_V > 3$. When the alignment was assumed to be independent on A_V , the anti-correlation was not observed. Recently, Pelkonen, Juvela & Padoan (2007) extended this work and refined the calculation of polarization degree introducing the radiative transfer properly. In that work, the decrease in the alignment efficiency arises without any *ad hoc* assumption. The alignment efficiency decreases as the radiative torques become less important in the denser regions. However, it is still not clear the role of the magnetic field topology and the presence of multiple cores intercepted by the line of sight on the decrease of polarization degree.

In this work we attempt to extend the previously cited studies improving and applying the CF method for different situations. For that, we studied both sub and super-Alfvénic models, to study the role of the magnetic field topology in the observed polarization maps. We simulate different observational resolutions in the calculations of polarization maps and provide combined statistical analysis for both dust absorption and emission maps. We also present statistics based methods to characterize the turbulence and magnetic properties from polarization maps. We performed numerical simulations of magnetized turbulent plasma with higher resolution, which are described in Sec. 2. From the data, we computed “observable” polarization maps, as shown in Sec. 3. We then present the statistics and spatial distributions of angle and polarization degree for different models in Sec. 4. In Sec. 5 we propose the generalized equation for the CF method and compare it with the expected values to study its validity. In Sec. 6, we discuss the improved procedures of polarization vector statistics, which allow observers to characterize the mean and fluctuating magnetic field of the cloud. We also discuss the applicability of our approach for polarized molecular and atomic lines, and compare the results with previous works. Our summary is provided in Sec. 7.

2. Numerical Simulations

The simulations were performed solving the set of ideal MHD equations, in conservative form, as follows:

$$\frac{\partial \rho}{\partial t} + \nabla \cdot (\rho \mathbf{v}) = 0, \quad (1)$$

$$\frac{\partial \rho \mathbf{v}}{\partial t} + \nabla \cdot \left[\rho \mathbf{v} \mathbf{v} + \left(p + \frac{B^2}{8\pi} \right) \mathbf{I} - \frac{1}{4\pi} \mathbf{B} \mathbf{B} \right] = \rho \mathbf{f}, \quad (2)$$

$$\frac{\partial \mathbf{B}}{\partial t} - \nabla \times (\mathbf{v} \times \mathbf{B}) = 0, \quad (3)$$

with $\nabla \cdot \mathbf{B} = 0$, where ρ , \mathbf{v} and p are the plasma density, velocity and pressure, respectively, \mathbf{B} is the magnetic field and \mathbf{f} represents the external acceleration source, responsible for the turbulence injection. For molecular clouds, we may assume that the ratio of dynamical to radiative timescales is very large. Under this assumption, the set of equations is closed by an isothermal equation of state $p = c_s^2 \rho$, where c_s is the speed of sound. The equations are solved using a second-order-accurate and non-oscillatory scheme, with periodic boundaries, as described in Kowal, Lazarian & Beresniak (2007).

Initially, we set the intensity of the x-directed magnetic field \mathbf{B}_{ext} and the gas thermal pressure p . This allows us to obtain sub-Alfvénic or super-Alfvénic, and subsonic or supersonic models.

The turbulent energy is injected using a random solenoidal function for \mathbf{f} in Fourier space. This, in order to minimize the influence of the forcing in the formation of density structures. We inject energy at scales $k \propto L/l < 4$, where L is the box size and l is the eddy size of the injection scale. The rms velocity δV is kept close to unity, therefore \mathbf{v} and the Alfvén speed $v_A = B/\sqrt{4\pi\rho}$ will be measured in terms of the rms δV . Also, the time t is measured in terms of the dynamical timescale of the largest turbulent eddy ($\sim L/\delta V$).

We performed four computationally extensive 3D MHD simulations, using high resolution (512^3), for different initial conditions, as shown in Table 1. We simulated the clouds up to $t_{\text{max}} \sim 5$, i.e. 5 times longer than the dynamical timescale, to ensure a full development of the turbulent cascade. We obtained one subsonic and three supersonic models. One of the supersonic models is also super-Alfvénic. Each data cube contains information about parameterized density, velocity and magnetic field. As noted from Eqs. (1) and (2), the simulations are non self-gravitating and, for this reason, the results are scale-independent.

Regarding the gas distribution in each model we found an increasingly contrast for increasing sonic Mach number, independent on the Alfvénic Mach number. This result was also obtained, and studied with more details, in Kowal, Lazarian & Beresniak (2007). Subsonic turbulence show a gaussian distribution of densities, while the increased number

and strength of shocks in supersonic cases create more smaller and denser structures. In these cases, the density contrast may be increased by a factor of 100 - 10000 compared to the subsonic case. The magnetic field topology, on the other hand, depends on the Alfvénic Mach number. Sub-Alfvénic models show a strong uniformity of the field lines, while the super-Alfvénic case shows a very complex structure. Both effects, the density contrast and the magnetic field topology, may play a role on the polarimetric maps, as shown further in the paper.

3. Polarization maps

Here we focus on the determination of observable quantities from our synthetic maps. From the density and magnetic field cubes we created “plane of sky” maps for column density and the linear polarization vectors. From the velocity field cubes it was possible to obtain the rms velocity, which is necessary to test the CF method.

To create the polarization maps we assumed that the radiation is originated exclusively by thermal emission from perfectly aligned grains. The dust abundance is supposed to be linearly proportional to the gas density and, in this case, the total intensity may be assumed to be proportional to the column density. We also assumed that all dust particles emit at the same temperature.

In this work we assume the dust polarization to be completely efficient ($\epsilon = 1$), and perfect grain alignment. Under these assumptions, the local angle of alignment (ψ) is determined by the local magnetic field projected into the plane of sky, and the linear polarization Stokes parameters Q and U are given by:

$$\begin{aligned} q &= \rho \cos 2\psi \sin^2 i, \\ u &= \rho \sin 2\psi \sin^2 i, \end{aligned} \tag{4}$$

where ρ is the local density and i is the inclination of the local magnetic field and the line of sight. We then obtain the integrated Q and U , as well as the column density, along the LOS. Notice that, for the given equations the total intensity (Stokes I) is assumed to be simply proportional to the column density. The polarization degree is calculated from $P = \sqrt{Q^2 + U^2}/I$ and the polarization angle $\phi = \text{atan}(U/Q)$. Previous works (e.g. Ostriker, Stone & Gammie (2001)) obtained the polarization maps integrating all cells along the line of sight, in spite of the fact that the local density may be too low to present an observable dust component. In reality, dense dust clouds are surrounded by warmer and

rarefied regions, in which the dust component is negligible. To simulate this effect, we neglect any contribution for cells with density lower than an specific threshold, which depends on the model. The threshold for each model is arbitrarily chosen to keep the minimum column density, i.e. intensity, as 0.3 of its maximum.

In Figs. 1 and 2, we show the obtained maps of column density and the polarization vectors for Model 3. We used the two extreme orientations of the magnetic field regarding the LOS (0 and 90°). Clearly, as shown in Fig. 1, the external magnetic field oriented in the x-direction dominates the polarization process. Fluctuations on the polarization angle are seen within the condensations, which are dense enough to distort the magnetic field lines. In Fig. 2, since the magnetic field is oriented along the LOS, the polarization is due exclusively by the random field components. The dispersion of the polarization angle is large and the polarization degree is, in average, lower than obtained in Fig. 1. Similar results were obtained for Models 1 and 2. Even though presenting different magnetic to gas pressure fraction, all the sub-Alfvénic models present similar maps.

In Fig. 3, we show the column density and polarization maps of the super-Alfvénic case (Model 4), assuming the magnetic field perpendicular to the LOS. Here, the kinetic energy is larger than the magnetic pressure. As a consequence the gas easily tangles the magnetic field lines. The angular dispersion is larger and the polarization degree is smaller when compared to the sub-Alfvénic case. For the super-Alfvénic case, the orientation of the magnetic field regarding the LOS is irrelevant to the polarization maps.

The histograms of polarization angles are shown in Fig. 4. In the upper panel we show the histograms for the sub-Alfvénic (Models 1, 2 and 3) and the super-Alfvénic (Model 4) cases, with the mean magnetic field lines perpendicular to the LOS. The polarization angles present very similar distributions and almost equal dispersion for the sub-Alfvénic cases. This happens mainly because they do not depend on the density structures, but on the magnetic topology. Strongly magnetized turbulence creates more filamentary and smoother density structures (i.e. low density contrast) if compared to weakly magnetized models and, most importantly the magnetic field lines are not highly perturbed. For Model 4, the distribution is practically homogeneous, which means that the polarization is randomly oriented in the plane of sky. It occurs because the turbulent/kinetic pressure is dominant and the gas is able to easily distort the magnetic field lines.

In the bottom panel of Fig. 4 we show the polarization angle histograms obtained for Model 3 but for different orientations of the magnetic field. The dispersion of the polarization angle is very similar for inclination angles $\theta < 60^\circ$, and increases for larger inclinations. It may be understood if noted that the projected magnetic field $B_{sky} = B_{ext} \cos \theta$ is of order of the random component δB . It shows that the dominant parameter that differ the

distributions of ϕ is the uniform magnetic field projected in the plane of sky, and not the intensity of the global magnetic field.

Furthermore, the distribution of polarization angles may be used to determine if a sample of clouds in a given region of the ISM present sub or super-Alfvénic turbulence. Since it is very unlikely to have all clouds with mean magnetic field pointed towards the observer, one non-homogeneous distribution of ϕ would reveal a sub-Alfvénic turbulence.

4. Spectra and structure function of polarization angles

4.1. Spectra

In turbulence studies it is useful to calculate the density and velocity power spectra. It allows a better understanding and characterization of the energy cascade process and the correlation between different scales. In Fig. 5 we present the power spectra of the polarization angle for Model 3 with different inclination angles θ (*upper panel*), Model 4 with different θ (*middle panel*) and for the different models (*bottom panel*). The spectra were obtained for sizes smaller than $L/4$ to eliminate contaminations from the forcing at large scales. As the inclination angle θ increases, more power is found in smaller scales (larger k) and the spectrum becomes flatter.

Interestingly, spectrum slopes could be used for the determination of the magnetic field inclination. However, the same trend is found by increasing the sonic and Alfvénic Mach numbers, as seen in the bottom panel. The degeneracy between Alfvénic Mach number and the magnetic field inclination makes it impossible to correctly estimate β (or the mass-to-flux ratio) of a given cloud from polarimetric map spectra unless additional information regarding the orientation of the magnetic field is given. Possibly, a different statistical analysis should be used to bypass this problem. The study of the decorrelation between different scales may show more sensitivity to θ and M_A than spectra, as shown below.

4.2. Structure functions

The second order structure function (SF) of the polarization angles is defined as the average of the squared difference between the polarization angle measured at 2 points separated by a distance l :

$$\text{SF}(l) = \langle |\phi(\mathbf{r} + \mathbf{l}) - \phi(\mathbf{r})|^2 \rangle. \quad (5)$$

The structure functions calculated for the different models are shown in Fig. 6. In the upper panel we present the SFs obtained for Model 3 with different values of θ . As expected, all curves present a positive slope showing the increase in the difference of polarization angle for distant points. However, the small scales part of the SF presents a plateau extending up to $l \sim 4 - 5$ pix. This range corresponds to the dissipation region and may also be related to the smallest turbulent cells.

As shown in the polarization maps, we should expect an increase in the values of SF as θ increases because of the increase in the dispersion of polarization angles. From Fig. 6 (upper panel) it is noticeable the increasing profiles of the SFs. However, surprisingly, the obtained slopes are very similar. For an assumed relation $SF \propto l^\alpha$ we obtained $\alpha \sim 0.5$, for $3 < l < 20$ pix, independently on θ .

In the middle panel we show the structure functions for Model 4 with different θ . Here, the SFs are almost equal, as noticed by the spectra. We also obtained a very similar slope for the different values of θ . It shows that the slope is independent on θ .

In the bottom panel we show the SFs calculated for the different models with $\theta = 0$. It is noticeable the increase in the SF for higher Mach numbers. However, the slopes are notably different. The maximum slope is $\alpha \sim 1.1, 0.8, 0.5$ and 0.3 for Models 1, 2, 3 and 4, respectively. Observationally, the molecular cloud M17 shows $\alpha \sim 0.5$ up to $l = 3$ pc (Dotson 1996), which would be in agreement with a cloud excited by supersonic and sub(or critically)-Alfvenic turbulence.

From these results we could possibly indicate that SFs of polarization maps may be used for the determination of the magnetic field intensity. Associated to other analysis, as spectra and polarization angle histograms, it would be possible to determine also the magnetic field inclination regarding the LOS. However, a more detailed study, using more numerical simulations considering a large range of parameters, is needed to support these results.

4.3. Structure functions at small separations

As discussed above, the structure functions of polarization angles present a plateau at small scales. Possibly, if we had “pencil beam” observations, its range could reflect the size of the smallest turbulent cells ($l_{\text{cell}} = l_0$). Infinite resolution observations would measure a non-zero (due to the neighboring eddies discontinuity) and flat SF up to a scale $l \sim l_0$. For $l > l_0$ the SF would present a positive slope. However, could the flat part of the SF also be dependent on the observational resolution, instead of the turbulent structures exclusively?

To study this effect, we calculated the polarization maps considering different observational resolutions. From the original 512×512 polarization maps, which is assumed to be the real cloud, we create the “observed” maps considering beam sizes 2×2 , 8×8 and 32×32 pix. The polarization angle is obtained from the Q and U integrated over the neighboring cells, and the SFs for each resolution were obtained from Eq. (5). The obtained SFs are shown in Fig. 7, for B_{ext} perpendicular (upper panel) and parallel to the LOS (bottom panel).

In both plots, we show that the SF is dependent on the observational resolution. As a common result, lower observational resolution results in higher SF at small scales and lower SF at large scales. This is a result of the averaging of the polarization map in the beam size. In the small boxes we show the logarithm of the structure function, and the slopes for the lowest and highest resolutions, 0.35 and 0.50, respectively. Therefore, the observational resolution may influence the determination of the magnetic field from the slopes of SFs, and this method should be used carefully.

An interesting feature is the extended plateau at small scales. The SF present a plateau up to a limiting scale, and a positive slope at larger scales. Observationally, similar profiles were obtained by (Dotson 1996), which shows that the current results may be implemented by high resolution observations. The limiting scale is approximately the beam size $l \sim l_{\text{res}}$. Therefore, the obtained results show that the smallest turbulent cells are only detectable if the condition $l_{\text{res}} \ll l_0$ is satisfied in the observations. Lazarian, Vishniac & Cho (2004) estimated l_0 for MHD turbulence, considering the viscous and ion-neutral collision damping, as:

$$l_0 \sim \lambda_{in}^{3/4} \left(\frac{c_s}{v_L} \right)^{3/4} \left(\frac{c_A}{v_L} \right)^{1/4} L^{1/4} f_n^{3/4}, \quad (6)$$

where λ_{in} is the mean-free-path for ion-neutral collisions, v_L is the eddy velocity at the injection scale L and f_n is the fraction of neutral atoms. Considering $\lambda_{in} \sim 5 \times 10^{14}$ cm, $c_s/v_L \sim 0.1$, $c_A/v_L \sim 1$, $f_n \sim 1$ and $L \sim 100$ pc, we obtain $l_0 \sim 10^{-3}$ pc. This represents ~ 0.5 arcsec for the Orion Molecular Cloud. Considering the instruments available, the required resolution is a little larger than obtained using SHARP and SOFIA ($\sim 2 - 10$ arcsec), but could be reached by the sub-millimeter array (SMA) (~ 0.4 arcsec). Observations at high resolutions could then also help us to better understand the process occurring at scales smaller than l_0 . However, the outcome of observations is yet uncertain since Lazarian, Vishniac & Cho (2004) showed that the magnetic field structures may be complex even below this scale.

5. Polarization and CF technique

5.1. Polarization degree and column density correlation

Another interesting analysis is related to the correlation between the column density and the polarization degree. As noticeable from Figs. 1, 2 and 3, the polarization degree is smaller within high column density regions for all models. This result is supported by observations, and was detected for several objects (Matthews & Wilson 2002; Lai, Girart & Crutcher 2003; Wolf, Launhardt & Henning 2003). Typically, the polarization degree follows the relation $P \propto I^{-\gamma}$, where $\gamma \sim 0.5 - 1.2$ (Gonçalves, Galli & Walmsley 2005) and I is the total intensity. A possible explanation could be the change on dust size and geometry at denser regions. In this case they would be less effectively aligned in respect to the magnetic field (Hildebrand et al. 1999). Another possibility could be an increase on the thermal collisions with gas and other dust particles in high density clumps (Lazarian, Goodman & Myers 1997). However, our numerical simulations does not take into account such processes and, therefore, those could not be influencing our results.

In Fig. 8 we show the correlation between the polarization degree and the column density for Model 3, considering orientations of magnetic field regarding the LOS (*upper panel*). Also, we show the correlations for the different models, assuming the magnetic field at the plane of the sky (*bottom panel*). For all angles, the polarization of high column densities tend to decrease to the minimum value ($\sim 20\%P_{\max}$), which is the value obtained for the case of purely random magnetic component ($\theta = 90^\circ$). This minimum polarization degree should be zero for homogeneous density and random magnetic field. In inhomogeneous media it depends on the number of dense structures intercepted by the line of sight. The major contribution for the polarized emission comes from dense clumps, which are few along the LOS. This poor statistics results in a non-zero polarization degree. For the super-Alfvénic case, the contrast in density is larger as well as the number of high density structures. In this case, the polarization degree is smaller, as seen in Fig. 8. We obtain, as best fit for the plots, a correlation exponent $\gamma = 0.5$. Cho & Lazarian (2005), studying the radiative torque efficiency in the grain alignment process, found larger values for γ . If grain alignment is implemented properly, the value of γ should increase (see Cho & Lazarian [2005]), but it is out of the scope of this work. From the bottom panel, it is noticeable that for sub-sonic turbulence the polarization degree is large even for the higher column densities. It occurs because in the sub-sonic models the contrast in density is small and the simulated domain is more homogeneous. Also, the number of dense clumps, which are able to tangle the field lines, is reduced in the sub-sonic case. On the contrary, for the super-Alfvénic case we obtain a correlation similar to $\theta = 90^\circ$, i.e. purely random magnetic field components.

These results indicate that the decrease in the polarization degree observed in molecular clouds may be partially due to an increase in the random to uniform ratio of the magnetic field components. The higher density flows are able to easily tangle the magnetic field lines. On the other hand, in the low density streams outside the clumps the magnetic field tends to be more uniform and the polarization degree higher.

5.2. The CF technique

Chandrasekhar & Fermi (1953) proposed a method for estimating the ISM magnetic fields based on the dispersion of polarization angles and the rms velocity. Basically, assuming that the magnetic field perturbations are Alfvénic, i.e. $\delta v \propto \delta B \sqrt{\rho}$, and that the rms velocity is isotropic we have:

$$\frac{1}{2}\rho\delta V_{LOS}^2 \sim \frac{1}{8\pi}\delta B^2, \quad (7)$$

where δV_{LOS} is the observational rms velocity along the LOS. Using the small angle approximation $\delta\phi \sim \delta B/B_u$, it reduces to:

$$B_u = \xi \sqrt{4\pi\rho} \frac{\delta V_{LOS}}{\delta\phi}, \quad (8)$$

where ϕ is measured in radians and ξ is a correction factor (~ 0.5) (Zweibel 1990; Myers & Goodman 1991), which depends on medium inhomogeneities, anisotropies on velocity perturbations, observational resolution and differential averaging along the LOS.

Ostriker, Stone & Gammie (2001) noticed from their numerical simulations that the CF method (Eq. [7]) was a good approximation for the cases where $\delta\phi < 25^\circ$, i.e. when the uniform component of the magnetic field is much larger than the random components. This conclusion is expected from Eq. (7) since it is applicable only for small values of $\delta\phi$, due to the angular approximation.

If one wants to expand the applicability of the CF method for cases where the random component of the magnetic field is comparable to the uniform component, or for larger inclination angles, it is necessary to take into account two corrections in Eq. (7).

Firstly, we must introduce the total magnetic field projected in the plane of sky $B_{\text{sky}} \sim B_{\text{sky}}^{\text{ext}} + \delta B$, where $B_{\text{sky}}^{\text{ext}}$ represents the mean field component projected on the plane of sky.

We assume here, for the sake of simplicity, that δB is isotropic¹. Heitsch et al. (2001) substituted $\delta\phi$ in the CF equation by $\delta(\tan\phi)$, where $\tan\phi$ was calculated locally, to provide a correction for the small angle approximation. However, they showed that this case lead to an underestimation (by a factor of 100) of the magnetic field in super-alfvenic cases. It occurred because, as $|\phi| \rightarrow \pi/2$ it gives $B_{\text{CF}}^{\text{mod}} \rightarrow 0$. To avoid this, they introduced a correction, which was the geometric average of the standard B_{CF} and the modified value $B_{\text{CF}}^{\text{mod}}$. Here, we implement the correction of the small angle approximation in a simpler way. We assume that the $\delta B/B$ is a global relation and, in this case, we may firstly obtain the dispersion of ϕ and then calculate its tangent. Substituting $\delta\phi$ in Eq. (7) by $\tan(\delta\phi) \sim \delta B/B_{\text{sky}}$, we obtain the modified CF equation:

$$B_{\text{sky}}^{\text{ext}} + \delta B \simeq \sqrt{4\pi\rho} \frac{\delta V_{\text{los}}}{\tan(\delta\phi)}, \quad (9)$$

which is a generalized form of Eq. (7). As an example, if polarization maps give $\delta\phi \rightarrow \pi/4$, Eq. (8) gives $B \rightarrow \delta B$ and $B_{\text{u}} \rightarrow 0$. This is expected for $\theta \rightarrow 90^\circ$ or $M_A \gg 1$.

5.3. Effects of finite resolution

Here we assume the obtained cubes as the real clouds subject to observational studies. In the previous sections we presented the expected results considering infinite observational resolution. However, observational data analysis may be biased by the limited instrumental resolution. Therefore, we must understand its role on the statistical analysis of the measured parameters.

We applied Eq. (8) to our simulated clouds, taking into account the effects of finite resolution. Here, we intended to determine the role of the resolution on the determination of the magnetic field strength from the CF method. We calculated the average of the density weighted rms velocity along the LOS (δV_{los}) and the dispersion of the polarization angle ($\delta\phi$) within regions of $R \times R$ pixels. To simulate a realistic cloud we chose the mean magnetic field intensities given in Table 2.

In Fig. 9 we show the averaged values of the obtained magnetic field for different map resolutions (255^2 , 31^2 and 7^2 pixels) for Model 3 with different inclinations of the magnetic

¹This assumption is not exact since the magnetic field fluctuations also show anisotropic structures regarding the mean magnetic field. Moreover, it was shown that the anisotropy is scale-independent (Lazarian & Pogosyan 2000; Esquivel & Lazarian 2005).

field. For all inclinations, coarser resolution calculations from the CF method tend to overestimate the magnetic field intensity. Finer resolutions result in the convergence to the actual values B_{sky} .

This trend is seen for different inclinations and models. The following equation seems to best fit this behavior:

$$B_{\text{CF}} = B_{\text{CF}}^0 \left(1 + \frac{C}{R^{0.5}} \right), \quad (10)$$

where R represents the observational resolution (total number of pixels), C and B_{CF}^0 are constants obtained from the best fitting. B_{CF}^0 represents the value of B_{CF} for infinite resolution observations, i.e. the best magnetic field estimation from the CF method. Eq. (10) is shown as the dotted lines in Fig. 9.

In Fig. 10 we show the magnetic field obtained from Eq. (8) for the different models with $\theta = 0$. The dotted lines represent the best fitting using Eq. (10).

The fit parameters, as well as the expected values of the magnetic field from the simulations for all models, are shown in Table 2. Here, the magnetic fields are given in units of the mean field B_{ext} . Since the simulations are scale independent, one could choose values of B_{ext} to represent a real cloud, in accordance with the parameters of Table 1. As an example, assuming a cloud with $n_{\text{H}} = 10^3 \text{cm}^{-3}$ and $T = 10\text{K}$, and $\beta = 0.01$ (Model 3), we get $B \sim 50\mu\text{G}$. Choosing differently the density, temperature or the model given by the simulations, i.e. β , we obtain a different mean magnetic field. The obtained parameter C is very similar for the different inclinations, but are different depending on the model, mainly because it is related to the scale on which the dispersion of the polarization angle changes. Since C seems to depend on the model and not on the inclination it could also be used by observers to infer the physical properties of clouds from polarization maps.

It is shown that B_{CF}^0 decreases as θ increases but do not reach zero as would be expected from $B_{\text{sky}}^{\text{ext}}$. However, if we compare the magnetic field strength obtained from the CF method with the total magnetic field (last column of Table 2) as proposed in Eq. (8), the convergence between the estimative and the actual values is much better. The error ($\epsilon = [\log(B_{\text{CF}}^0) - \log(B)]/\log(B_{\text{CF}}^0)$) using this method is $< 20\%$ considering all cases, validating the CF method under the assumptions used for Eq. (8).

As a practical use, observers could obtain polarimetric maps of a given region of the sky for different observational resolutions (e.g. changing the resolution via spatial averaging). Using the CF technique for each resolution and, then apply Eq. (9) to determine the asymptotic value of the magnetic field projected into the plane of sky B_{CF}^0 .

5.4. Polarization of stellar radiation

Dense cloud envelopes and diffuse clouds typically present very weak or no far-IR and sub-mm dust emission. In these cases, it is very difficult to obtain polarimetric maps from dust emission and other methods are necessary. Some of these clouds are known to intercept rich clusters of stars. IR, optical and ultraviolet (UV) emissions from these stars suffer extinction by the dust component of the intercepting clouds and, as a consequence, the detected stellar radiation may be polarized.

Absorption polarization maps are considered “infinite resolution” measurements of polarization vectors and can be very useful on the study of the magnetic field of the ISM. However, since it depends on the stellar background, detections are rare and the polarization maps are sparse.

To test if the current absorption polarization maps are statistically relevant, as well as the applicability of the CF technique for these type of observation, we simulated the polarization of background stars in our cubes. Assuming our cubes to be 1 arcmin^2 of the sky, and using the density estimative of $10^3/\text{arcmin}^2$ for our Galaxy (Garwood & Jones 1987), we recalculated the polarization maps of 10^3 randomly positioned stars. Each star is assumed to originate an unpolarized total intensity S , which is absorbed by the dust component intercepting the line of sight. At each cell, we compute the absorbed intensities δI_x and δI_y , which depend on the local magnetic field orientation. Again, as in the calculation of the emission maps, we assume maximum efficiency in the polarization by the dust. After integration, the total absorptions I_x and I_y are used to obtain Q and U . The obtained polarization angle is then rotated by 90° (opposite polarization) in order to be compared with the emission polarimetric maps.

In Fig. 11 we illustrate the obtained results. We exemplify the obtained maps with a zoomed clumpy region (100×100 pixels) of Model 3 with $\theta = 90^\circ$ (upper panel). Here, it is shown that just a few stars (< 50) are detected.

To test the predictions of the magnetic field proposed in this work, we calculated the dispersion and the structure function of the polarization angles. In the bottom panel of Fig. 11 we show the histogram of ϕ , and its structure function (squares), for Model 3 with $\theta = 0^\circ$. We compared it with the dust emission SF (solid line). The structure functions seem very similar but, due to the small number of stars, the dispersion in the SF for absorption is large. In this case, the SFs from absorption maps may present too large uncertainties, which make difficult the analysis of the magnetic field from SF slopes.

An alternative would be the use of the improved CF technique presented in Sec. 5. We applied the CF method to the absorption polarization maps of Model 3, with $\theta = 0^\circ$,

which resulted in $B_{CF}^{\text{abs}} = 550 \pm 126 \mu\text{G}$. This value is comparable to the result obtained from the emission polarimetric maps ($B_{CF}^{\text{em}} = 464 \pm 45 \mu\text{G}$). Even with a small number of stars, the obtained result is similar to the finest resolution case of polarized emission. It occurs because the stars act as single pixel measurements and there is no averaging of ϕ within the observational beam size. The down-side of this technique is its higher noise.

Currently there are few observed polarization maps available from extinction of background stars. Fortunately, some projects are being implemented and promise to bring us complete sets of polarization maps of background stars, which would be compared to the presented results, like the Galactic Plane Infrared Polarization Survey (Shiode et al. 2006). However, we believe that joint analysis of both, emission and absorption, polarization maps can provide a more complete understanding of the magnetic field in dense and diffuse regions of the ISM.

6. Discussions

Emission and extinction polarimetric measurements provide an unique technique for the study of the magnetic field, projected into the plane of sky, in molecular clouds. Synthetic extinction maps depend on additional assumptions about the stellar population and may be more explored in a future work. In this work we focused on providing synthetic emission polarimetric maps, as well as different statistical analysis that could be used in the future by observers to infer the physical properties of the studied region. The physical interpretations of our results, as well as the comparisons with previous theoretical works, are given as follows.

6.1. Our models

In this work we presented four different models: (1) $\beta = 1.0$, $M_S = 0.7$ and $M_A = 0.7$, (2) $\beta = 0.1$, $M_S = 2.0$ and $M_A = 0.7$, (3) $\beta = 0.01$, $M_S = 7.0$ and $M_A = 0.7$ and (4) $\beta = 0.1$, $M_S = 7.0$ and $M_A = 2.0$. Similar studies provided by Ostriker, Stone & Gammie (2001) characterized different models by their pressure ratio. However, our results show completely different polarization maps for the two coincident β -value models. This because the super-Alfvénic flows tend to tangle the magnetic field lines, what is not seen in the sub-Alfvénic models (Model 2), even with similar pressure ratio.

The super-Alfvénic case shows a randomly distributed column density maps, with high contrast between the denser and rarefied regions. On the other hand, sub-Alfvénic cases are more filamentary, with contrasts increasing with the sonic Mach number. This general

picture is independent on the angle between the external mean magnetic field and the LOS θ . However, for B_{ext} nearly parallel to the LOS, the observed polarization will mostly be due to the random fluctuation component δB . This effect is noticeable comparing Figs. 1 and 2.

We see that for sub-Alfvénic turbulence the large scale density enhancements are mostly parallel to the mean magnetic fields, with exception to the very dense cores, which can easily change the orientation of the magnetic field. As a consequence, polarization maps will present dense structures mostly aligned with the mean magnetic field. This effect also play a role on the generation of the polarization maps. Since we integrate the polarization vectors along the LOS, the low density cells will systematically increase the homogeneous contribution, as well as the resulting polarization degree. To avoid this effect, we disregarded the contribution from low density cells using a threshold, which depends on the model used. For the models where the magnetic field is oriented parallel to the LOS, the polarization maps will show polarization vectors randomly oriented in respect to the density structures. It reveals the degeneracy on the polarimetric maps between the super-Alfvénic models with those with B nearly parallel to the LOS.

6.2. Polarization degree versus emission intensity

The polarization maps showed that the polarization degree is anti-correlated to the column density, in exception to the subsonic case. This result is in agreement with the observations, which revealed “polarization holes” associated to the dense cores for most of the regions observed.

Observationally, Wolf, Launhardt & Henning (2003) showed that the polarization maps of molecular clouds follow the relation $P \propto I^{-\gamma}$, with $\gamma \sim 0.5 - 1.2$. The same trend is observed from polarized extinction of background stars (Arce et al. 1998). It was proposed that this behavior occurs due to changes on dust properties inside denser cores, or even by an increase in thermal pressure, causing depolarization. Cho & Lazarian (2005) studied the role of the radiative torques on the grain alignment at dense cores and obtained $\gamma \sim 0.5 - 1.5$, depending on the dust size distribution.

Padoan et al. (2001) obtained a similar behavior from their numerical simulations of protostellar cores, though for only three dense cores of one single simulation. They assumed a cut-off on grain alignment efficiency for $A_V > 3\text{mag}$. For their model, if the alignment efficiency is independent on A_V , the polarization degree was shown to be independent on the column density. Pelkonen, Juvela & Padoan (2007) extended this work, improving the

radiative transfer. They naturally obtained a decrease in the grain alignment at denser regions, explaining the lower degree of polarization.

In our models, we assumed perfect grain alignment (independent on A_V). Therefore, the depolarization is exclusively due to the dispersion increase of the polarization angles in denser regions. We obtained $\gamma \sim 0.5$ for Models (2) and (3), but no correlation (i.e. $\gamma \sim 0$) was found for Models (1) and (4). For Model (1), even the densest cores are unable to tangle the magnetic field lines and the polarization degree is homogeneously large. For Model (4), we have the opposite situation. The super-Alfvénic turbulence causes a strong dispersion of the magnetic field even at the less dense regions. For this case, the polarization degree is low everywhere. For Models (2) and (3), the turbulence is unable to destroy the magnetic field structure, but is able to create the dense cores by shocks. The cores are dense enough to drag the magnetic field lines and to increase the local M_A .

Possibly, our results differ from the obtained by Padoan et al. (2001) because of: i - numerical resolution, ii - M_A , and iii - self-gravity. We used 512^3 simulations (instead of a 128^3) and, as a result, our magnetic field structure is less homogeneous and the density contrast is higher. The larger complexities present in our cubes increase the effect described in the previous paragraph. Padoan et al. (2001) and Pelkonen, Juvela & Padoan (2007) used a single, super-Alfvénic, model. We showed that the polarization maps for M_A present a flat $P \times I$ correlation. Finally, self-gravity causes the collapse of the denser regions compressing the magnetic field within these cores. As a consequence, if no strong diffusion takes place, the polarization degree tends to grow. As a future work, we plan to study properly the depolarization at dense cores considering the grain alignment process and self-gravity.

6.3. Statistics of polarization angles

We found that the distributions of polarization angles of sub-Alfvénic models are similar, even for different magnetic to gas pressure ratios. However, the dispersion of angles increases with M_A and with the inclination of the external magnetic field regarding the line of sight (θ). Actually, we noticed that the critical parameter is the Alfvénic Mach number considering the magnetic field component projected into the plane of sky (i.e. $M_A^{\text{sky}} = \delta v \sqrt{4\pi\rho} / B_{\text{sky}}$). We can compare these results with Padoan et al. (2001) and Ostriker, Stone & Gammie (2001). The first used one single super-Alfvénic model, and obtained irregular (flat) distributions of polarization angle. The latest analysed supersonic models for $\beta = 0.01, 0.1$ and 1.0 . They obtained clearly gaussian distributions for $\beta = 0.01$, with increasing dispersion for larger inclinations. Also, they obtained flatter distributions as β increases (i.e. as the Alfvénic Mach number increases). These are all in agreement with our results.

On the other hand, the power spectra analysis was showed to depend on the sonic Mach number. The spectra of the polarization angles show an increase in the power of small scales for increasing M_S . This occurs due to the amplification on the perturbations of the smallest scales for stronger turbulence. However, the same behavior is seen varying the inclination of the mean magnetic field. In this sense, there is a degeneracy between the Alfvénic Mach number and the orientation of the magnetic field. In this sense, structure functions of the polarization angle showed to be useful to avoid this degeneracy.

The sub-Alfvénic models presented SFs with slope $\alpha \sim 0.5$ ($SF \propto l^\alpha$), independent on the magnetic field orientation. On the other hand, the super-Alfvénic model presented flatter SFs ($\alpha \sim 0.3$). Therefore, we could conjecture that it could be possible to obtain the mean magnetic field intensity, independently on its orientation regarding the LOS, from the SF slopes. Needless to say that more models are needed to confirm this possibility.

Besides, SFs can potentially be used to study the turbulence eddies. Its flat profile at small scales may provide informations about the amplitude and size of the smallest turbulence cells. However, we showed that the results are affected by the observational resolution.

6.4. Improved CF technique

The CF method has been proven an useful tool for the determination of the magnetic field in the ISM. We studied its validity using the obtained polarization maps from our models. Ostriker, Stone & Gammie (2001) proposed that the CF method would only be applicable in restricted cases, in which the dispersion of the polarization angle is small ($< 25^\circ$). It is consistent with the original approximations involving the derivation of the CF equation. We derived a generalized formula for the CF method, based on the same assumptions of the original work (Chandrasekhar & Fermi 1953), but that accounts for larger dispersion models. Basically, we assume that the perturbations are Alfvénic and that we have an isotropic distribution of δV . We, for the first time, successfully applied this equation to the super-Alfvénic and large inclination models.

We also studied dependency of the CF method and the observational resolution. As also shown by Ostriker, Stone & Gammie (2001) and Heitsch et al. (2001), the CF method overestimates the magnetic field for coarser resolutions. Therefore, we propose a general equation to fit the observational data considering maps with different resolution. The asymptotic value of the given procedure provides the “infinite resolution” measurement from the CF method and is consistent with the expected values from the simulations.

As stated before, a possible limitation in the presented model is the absence of self-

gravity effects. At the denser regions, the magnetic field configurations may possibly be different as the cloud collapses and drags the field lines. This process is responsible for the hour-glass structures observed in several gravitationally unstable clouds (e.g. Vallée & Fiege 2007). As a consequence, self-gravity increases the magnetic field locally and reduces the dispersion of the polarization angles within the dense clumps. To test the stability of the dense clumps in our simulations we may estimate the Jeans length ($\lambda_J = c_s \sqrt{\pi/G\rho}$). For the parameters chosen in Section 5.3, the denser structures, considering all models, are characterized by $l_{\text{core}} \sim 0.1 - 0.5\text{pc}$, $n_{\text{core}} \sim 10^{5-6}\text{cm}^{-3}$ and $T = 10 - 100\text{K}$, resulting in $\lambda_J \sim 0.1 - 1\text{pc}$. Therefore, since $l_{\text{core}} \sim \lambda_J$, the denser structures may be unstable, at least for the given parameters. On the other hand, self-gravity plays a role at small regions and may not be statistically important for the previous results (except for the $P \times I$ correlation) as we studied regions much larger than the very dense clumps. We plan to study the effects of self-gravity on the obtained results in a further work.

6.5. Sub-Alfvenic versus super-Alfvenic turbulence

The ratio of thermal gas to magnetic pressures (β) is typically used as the dominant parameter on the characterization of the degree of magnetization of a cloud. In this sense, systems with similar β values should present similar distribution of structures and dynamics. However, we showed that the sonic (M_S) and Alfvenic (M_A) Mach numbers, which quantify the ratio of the kinetic to the thermal and magnetic pressures, respectively, divide the models in different regimes. For the case of polarization vectors, our simulations showed that M_A is decisive.

For clouds with $M_A < 1$, the gas motions excited by turbulence are confined by the magnetic field and are not able to change its configuration. Actually, the perturbations in the magnetic field occur, but are small compared to the mean field ($\delta B \ll B_m$). In this case, the polarization vectors are uniform, as shown in Fig. 4. For $M_A > 1$, the magnetic pressure is small compared to the kinetic energy of the turbulent gas and the mean magnetic field can be easily distorted. As a consequence, the polarization maps would show large dispersion of ϕ .

Obviously, a large dispersion of ϕ can also be related to a projection effect. If the mean magnetic field is projected along the line of sight ($\theta \sim 90^\circ$), only the small perturbations δB will be seen as the polarization vectors. However, considering a large number of clouds, there is a very low probability for all to present $\theta \sim 90^\circ$. In this case, if observations systematically show very large dispersions of ϕ , it means that the turbulence in the ISM may be typically super-Alfvenic. Otherwise, the ISM then presents sub(quasi)-Alfvenic turbulence.

Observations of a given cloud could then be compared to our Fig. 4 to determine under which regime the turbulence is operating. It is particularly interesting since the ratio of magnetic to turbulent energy in the ISM is still subject of controversy (Padoan & Norlund 2002; Girart, Rao & Marrone 2006).

6.6. Procedure for observational data analysis

The number of simulations presented in this work, as well as the numerical resolution, must be increased in future works. In any case, from the models we have, we intend to provide observers with a straightforward procedure to characterize the magnetic field and turbulence properties of molecular clouds.

Firstly, from the polarization maps of a given region one should obtain the second order structure function of the polarization angle. From the SF, it is possible to characterize the turbulent cascade and the magnetic field. The extension of the flat profile at small scales give the turbulence cut-off scale. On the other extreme, the flat profile at large scales indicate the energy injection lengths. From the maximum slope of $SF \propto l^\alpha$, it is possible to determine the averaged Alfvénic Mach number and, as a consequence, the magnetic field intensity.

Another method to obtain the magnetic field intensity is based on the CF technique. From the observed velocity dispersion it is possible to estimate the amplitude of the random component of the magnetic field from Eq. (7). The total magnetic field is then obtained from Eq. (9), using the dispersion of the polarization angle. To avoid the dependence on the observational resolution, it is suggested to evaluate the dispersion of the polarization angle for different resolutions (which may be simulated by averaging neighboring vectors of the polarization maps) and determine the asymptotic total magnetic field from Eq. (10). Finally, subtracting the total field by the random component, it is possible to determine the mean magnetic field projected in the plane of sky.

Also, combining the mean magnetic field obtained from both methods, it is possible to estimate the angle between the mean magnetic field and the LOS.

6.7. Grain alignment

Although it was not considered in the present calculations, a correct treatment of grain alignment is needed for a full understanding of the polarization in molecular clouds. For instance, we showed that the polarization degree is anti-correlated with the column density with slope $\gamma \sim -0.5$, while observations sometimes give $\gamma < -1.0$ (Gonçalves, Galli & Walmsley

2005). This difference is related with the alignment efficiency at different regions of the cloud (Cho & Lazarian 2005).

The theory of grain alignment has developed fastly during the past decade (see Lazarian [2007]). It is currently believed that radiative torques play a major role on the alignment process and it strongly depends on A_V (see Lazarian & Hoang [2007]). With increasing extinction ($A_V > 2$), the radiative torques are less effective and only large grains are aligned. All in all, both observations (Arce et al. 1998; Whittet et al. 2008) and theory (Hoang & Lazarian 2008), suggest that there is a range of A_V for which our assumptions are correct. It might happen that subsonic mechanical alignment of irregular grains, introduced in Lazarian & Hoang (2007b), extends the range of A_V over which grains are aligned when compared to the estimates based on radiative torques only.

The observed band is also selective regarding the dust sizes and different bands reveal the polarization of different dust components. All these effects will be included in a future work, and a more realistic study of the polarization intensity distribution will be obtained.

6.8. Polarization from molecular and atomic lines

In the present work we focused on calculating synthetic polarization maps of FIR emission from dust particles, which were assumed to be perfectly aligned with the magnetic field. Unfortunately, due to inefficient grain alignment at the dense cloud cores, the dust polarization degree may decrease and different methods have to be used.

The polarization of molecular lines have been shown to be an additional tool for the study of the magnetic fields in the ISM (Girart, Crutcher & Rao 1999; Greaves, Holland & Dent 2002; Girart et al. 2004; Cortes, Crutcher & Watson 2005). Molecules are present in the dense and cold cores of the clouds and may be detected by thermal line emissions. Polarimetric maps of molecular emission can be used on the study of regions with $A_V > 10$, and can be directly associated with the Zeeman measurements. Based on the Goldreich-Kylafis effect (Goldreich & Kylafis 1981, 1982), the molecular sublevel populations will present imbalances due to the magnetic field, generating polarized rotational transitions. However, the survival of molecules depend on restrict conditions, as for $A_V > 10$ molecules may be frozen into dust particles. Another difficulty regarding this method is the fact that the GK effect generates polarization either parallel or perpendicular to the magnetic field lines, making the polarization maps.

On the other hand, polarized scattering and absorption from atoms and ions provide information about the magnetic field in warm and rarefied regions, like the diffuse ISM and

the intergalactic medium.

Polarization arising from aligned atoms and ions is a new method (Yan & Lazarian 2007a). Unlike molecular lines that live in the excited state long enough to be imprinted by the magnetic field, the atomic excited states are short lived and tend to decay in timescales shorter than the Larmor precession of the atom. However, species with fine and/or hyperfine structure of ground or metastable states can be aligned. This fact opens new horizons for polarimetric studies of magnetic fields (Yan & Lazarian 2006, 2007a,b).

It is useful to comment here that the results shown in this work are also valid for the observed polarization maps of molecular and atomic emission lines. This because the assumptions made for the calculations disregard any special consideration about the emitting species, which could be atoms, molecules or dust particles.

Also, it is worth mentioning that these techniques are either a substitute, for regions where no FIR dust emission is detectable, or complementary to the dust polarized emission but at different wavelengths (e.g. optical and UV radiation). Depending on the A_V range considered, polarization of atoms and molecules may complement the dust emission and absorption maps, which are usually much more detailed.

6.9. Comparison with previous works

In this work we studied of polarization maps and its applicability on the determination of magnetic fields in molecular clouds based on numerical simulations. Here we compare the obtained results with the previous theoretical works.

Ostriker, Stone & Gammie (2001) performed numerical simulations, with 256^3 resolution, considering plasma β values 0.01, 0.1 and 1.0. Their results showed homogeneous polarization maps for $\beta = 0.01$ (strongly magnetized turbulence), and a complex distribution of polarization vector for $\beta = 0.1$ and 1.0 (weakly magnetized turbulence). They also obtained an increase in the dispersion of polarization angles with the increase of the external magnetic field inclination regarding the line of sight. These results are in agreement with our models, except for the fact that two of our models with equal β presented completely different polarization maps. This because the β value does not reveal how the magnetic field lines respond to the turbulence. The Alfvénic and sonic Mach numbers reflect how strong is the turbulent pressure compared to the magnetic and thermal pressures, respectively.

They obtained a higher polarization degree for $\beta = 0.01$, obviously because of the magnetic field intensity, but larger values of P for larger column densities (i.e. for larger

I), in disagreement with observations. We believe that this was caused by their method for obtaining the polarization degree. They obtained the integrated Stokes parameters, weighted by local density, for all cells along the LOS. We, on the other hand, used a threshold on density to avoid the contribution of very rarefied regions (where the magnetic field structure is systematically more uniform). Padoan et al. (2001) focused their work on the polarization of dust emission from dense cores. They implemented a more realistic calculation of the polarization degree based on the efficiency of the alignment for different values of A_V . In this case, they were able to obtain a decreasing polarization degree with the total intensity related to the grain properties, and not to the statistics of polarization vectors along the line of sight. We also believe that the numerical resolution may be playing a role on the polarization degree. More refined simulations systematically result in more complex structures for density and magnetic field lines. As a consequence, the alignment vectors along the line of sight present larger dispersion resulting in a lower polarization degree.

We found no previous theoretical work presenting an extended statistical analysis considering all the PDF, Spectra and Structure Function of polarization angle, and therefore no comparison can be made.

Ostriker, Stone & Gammie (2001) and Padoan et al. (2001) also tested the CF technique using their simulations, considering Eq. (8). They obtained good agreement, with a correction factor of ~ 0.5 , between the calculated estimations and the expected values only for the models with $\delta\phi < 25^\circ$. Heitsch et al. (2001) presented an extended analysis using a larger number of models, with different physical parameters and numerical resolutions (including 1 model with 512^3 resolution). They also studied the effects of observational resolution on the obtained maps. They concluded that coarser resolutions result in more uniform polarization vectors. As a consequence, the CF method overestimates the magnetic field intensity. This is in full agreement with our results. They also tested the reliability of the CF technique in weakly magnetized clouds. They proposed the modified equation $B_{CF} B_{CF}^{mod} = 4\pi\rho[\delta v_{LOS}/\delta(\tan\phi)][1 + 3\delta(\tan\phi)^2]^{1/2}$,² which gave good results compared with the expected values for their models, with discrepancies of a factor < 2 .

We tested their equation to our models 3 and 4 with $\theta = 0$, representing a strong and weakly magnetized cloud, respectively. For Model 3, the obtained value is in agreement with that shown in Table 2. The ratio between the two measurements is $B_{CF}^{mod}/B_{CF}^0 = 0.9$. For Model 4, the proposed equation underestimates the magnetic field, and compared to with our method it gives $B_{CF}^{mod}/B_{CF}^0 \sim 0.3$. Despite of the few simulations available for compariron,

²Here, B_{CF} is the value obtained using the standard CF equation, and B_{CF}^{mod} is the corrected value proposed by Heitsch et al. (2001).

their method seems to systematically underestimate the magnetic field intensity. More tests are needed to determine which method may give the best results.

Furthermore, even though not addressed by Heitsch et al. (2001), we studied the dependence of the polarization angles and the CF technique with the inclination of the magnetic field regarding the LOS. We showed that there is a degeneracy between the results of weakly magnetized clouds and strongly magnetized clouds with high θ . The modified CF formula presented in this work gave good results for all cases.

As discussed before, even though not taking into account the self-gravity in our simulations it mostly induces changes at small scales, as noted by Heitsch et al. (2001). As a result, they showed the CF technique to be insensitive to self-gravity.

7. Summary

In this work we presented turbulent 3-D high resolution MHD numerical simulations in order to study the polarized emission of dust particles in molecular clouds. We obtained synthetic dust emission polarization maps calculating the Stokes parameters Q , U and I assuming perfect grain alignment and that the dust optical properties are the same at all cells. Under these conditions, we were able to study the polarization angle distributions and the polarization degree for the different models and for different inclinations of the magnetic field regarding the LOS. As main results, we:

- obtained an anti-correlation between the polarization degree and the column density, with exponent $\gamma \sim -0.5$, related to random cancelation of polarization vectors integrated along the LOS;

- showed that the overall properties of the polarization maps are related to the Alfvénic Mach number and not to the magnetic to gas pressure ratio.

- calculated the spectra and structure functions of the polarization angles, and obtained degenerate conclusions for the Alfvénic Mach number and the angle between the magnetic field and the LOS;

- presented a generalization of the CF method, which showed useful for: i- the determination of the total magnetic field projected in the plane of sky, and ii- the separation of the two components B_{sky} and δB ;

- studied the effects of different observational resolutions on the CF method. We pre-

sented an empirical equation to determine the correct magnetic field from different resolution measurements;

- studied the effects of different observational resolutions on the structure function of the polarization angle. We discuss the applicability of SFs for the determination of turbulent cut-off scales.

These results represent important tools for present and future polarimetric FIR observational studies. In the future it would be necessary to increase the number of simulated models, with different physical parameters and with better resolutions, to test these conclusions. It would also be interesting to implement the grain alignment processes properly and study their effects on the obtained results. Using more computational models it will be possible to test the proposed method to remove the degeneracy between the Alfvénic Mach number and the angle between the magnetic field and the LOS. This would also help us to provide the observers a large number of simulated clouds that could be used as benchmarks.

D.F.G., A.L. and G.K. thank the financial support of the NSF (No. AST0307869), the Center for Magnetic Self-Organization in Astrophysical and Laboratory Plasmas and the Brazilian agencies FAPESP (No. 06/57824-1 and 07/50065-0) and CAPES (No. 4141067).

REFERENCES

- Arce, H. G., Goodman, A. A., Bastien, P., Manset, N. & Sumner, M. 1998, *ApJ*, 499, 93
- Cortes, P. C., Crutcher, R. M. & Watson, W. 2005, *ApJ*, 628, 780
- Cho, J. & Lazarian, A. 2005, *ApJ*, 631, 361
- Chandrasekhar, S. & Fermi, E. 1953, *ApJ*, 118, 113
- Crutcher, R. M. 1999, *ApJ*, 520, 706
- Crutcher, R. M., Roberts, D. A., Troland, T. H. & Goss, W. M. 1999, *ApJ*, 515, 275
- Dolginov, A. Z. & Mytrophanov, I. G. 1976, *Ap&SS*, 43, 257
- Dotson, J. 1996, *ApJ*, 470, 566
- Draine, B. T. & Weingartner, J. C. 1996, *ApJ*, 470, 551
- Draine, B. T. & Weingartner, J. C. 1997, *ApJ*, 480, 633

- Esquivel, A. & Lazarian, A. 2005, *ApJ*, 631, 320
- Garwood, R. & Jones, T. J. 1987, *PASP*, 99, 453
- Girart, J. M., Crutcher, R. M. & Rao, R. 1999, *ApJ*, 525, 109
- Girart, J., Greaves, J. M., Crutcher, R. M. & Lai, S.-P. 2004, *Ap&SS*, 292, 119
- Girart, J. M., Rao, R. & Marrone, D. P. 2006, *Science*, 313, 812
- Goldreich, P. & Kylafis, N. D. 1981, *ApJ*, 243, 75
- Goldreich, P. & Kylafis, N. D. 1982, *ApJ*, 253, 606
- Gonçalves, J., Galli, D. & Walmsley, M. 2005, *A&A*, 430, 979
- Greaves, J. S., Holland, W. S. & Dent, W. R. F. 2002, *ApJ*, 578, 224
- Heiles, C. & Troland, T. H. 2005, *ApJ*, 624, 773
- Heitsch, F., Zweibel, E., Mac Low, M. M., Li, P. S., & Norman, M. L. 2001, *ApJ*, 561, 800
- Hildebrand, R. H., Davidson, J. A., Dotson, J. L., Dowell, C. D., Novak, G., & Vaillancourt, J. E. 2000, *PASP*, 112, 1215
- Hildebrand, R. H., Dotson, J. L., Dowell, C. D., Schleuning, D. A. & Vaillancourt, J. E. 1999, *ApJ*, 516, 834
- Hoang, T. & Lazarian, A. 2008, *MNRAS*, in press
- Kritsuk, A. G., Norman, M. L., Padoan, P. & Wagner, R. 2007, *ApJ*, 665, 416
- Kowal, G., Lazarian, A. & Beresniak, A. 2007, *ApJ*, 658, 423
- Lai, S.-P., Girart, J. M. & Crutcher, R. M. 2003, *ApJ*, 598, 392
- Lazarian, A., Goodman, A. A. & Myers, P. C. 1997, *ApJ*, 490, 273
- Lazarian, A. & Pogosyan, D. 2000, *ApJ*, 537, 720
- Lazarian, A. & Cho, J. 2004, *Ap&SS*, 292, 29
- Lazarian, A., Vishniac, E. T. & Cho, J. 2004, *ApJ*, 603, 180
- Lazarian, A. 2007, *J. Quant. Spec. Radiat. Transf.*, 106, 225
- Lazarian, A. & Hoang, T. 2007a, *MNRAS*, 378, 910

- Lazarian, A. & Hoang, T. 2007b, *ApJ*, 669, 77
- Matthews, B. C. & Wilson, C. D. 2002, *ApJ*, 574, 822
- Myers, P. C. & Goodman, A. A. 1991, *ApJ*, 373, 509
- Ostriker, E. C., Stone, J. M. & Gammie, C. F. 2001, *ApJ*, 546, 980
- Padoan, P., Goodman, A., Draine, B. T., Juvela, M., Nordlund, A. & Rognvaldsson, o. E. 2001, *ApJ*, 559, 1005
- Padoan, P. & Norlund, A. 2002, *ApJ*, 576, 870
- Pelkonen, V.-M., Juvela, M. & Padoan, P. 2007, *A&A*, 461, 551
- Schleuning, D. A. 1998, *ApJ*, 493, 811
- Shiode, Joshua H., Clemens, D. P., Janes, K. A., Pinnick, A. & Taylor, B. 2006, *BAAS*, 209, 156
- Vallée, J. P. & Fiege, J. D. 2007, *AJ*, 134, 628
- Whittet, D. C. B., Hough, J. H., Lazarian, A. & Hoang, T. 2008, *ApJ*, in press
- Wolf, S., Launhardt, R. & Henning, T. 2003, *ApJ*, 592, 233
- Yan, H. & Lazarian, A. 2006, *ApJ*, 653, 1292
- Yan, H. & Lazarian, A. 2007a, *ApJ*, 657, 618
- Yan, H. & Lazarian, A. 2007b, astro-ph:0711.0926
- Zweibel, E. G. 1990, *ApJ*, 362, 545

Table 1: Description of the simulations - MHD, 512³

Model	P	B_{ext}	M_S^a	M_A^b	Description
1	1.00	1.00	0.7	0.7	subsonic & sub-Alfvenic
2	0.10	1.00	2.0	0.7	supersonic & sub-Alfvenic
3	0.01	1.00	7.0	0.7	supersonic & sub-Alfvenic
4	0.01	0.10	7.0	2.0	supersonic & super-Alfvenic

^asonic Mach number ($M_S = \langle v/c_S \rangle$)

^bAlfvenic Mach number ($M_A = \langle v/v_A \rangle$)

Table 2: CF method estimates

Model	$\theta(^{\circ})$	C	$B_{\text{CF}}^0/B_{\text{ext}}$	$B_{\text{sky}}^{\text{ext}}/B_{\text{ext}}$ ^a	$B_{\text{tot}}/B_{\text{ext}}$ ^b
3	0	20 ± 5	1.24 ± 0.09	1.00	1.25
3	30	24 ± 5	0.98 ± 0.08	0.87	1.11
3	45	25 ± 5	0.78 ± 0.07	0.71	0.96
3	60	33 ± 5	0.48 ± 0.05	0.50	0.75
3	90	31 ± 5	0.26 ± 0.03	0.00	0.24
1	0	7 ± 5	0.97 ± 0.08	1.00	1.11
2	0	10 ± 5	1.07 ± 0.07	1.00	1.16
4	0	34 ± 5	1.18 ± 0.07	1.00	1.41

^aMean field adopted for the model, projected into the plane of sky, i.e. $B_{\text{sky}}^{\text{ext}} = B_{\text{ext}} \cos \theta$

^bTotal field of the model, projected into the plane of sky, i.e. $B_{\text{tot}} = B_{\text{sky}}^{\text{ext}} + \delta B$

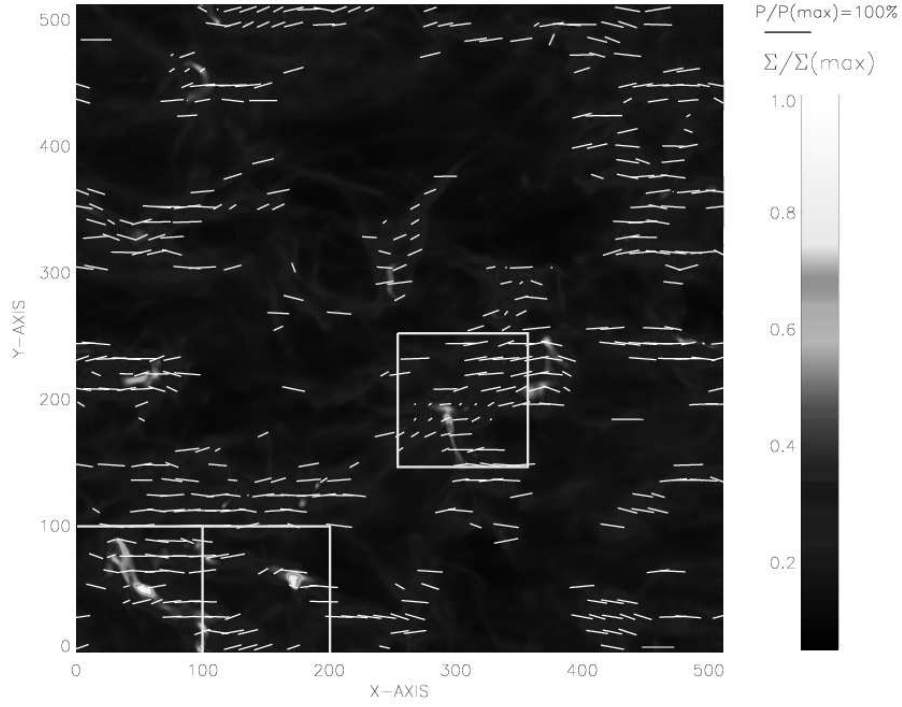


Fig. 1.— Polarization of emission and column density maps for Model 3 ($M_S \sim 7.0$ and $M_A \sim 0.7$) with \mathbf{B}_{ext} perpendicular to the line of sight. The complete map (512x512 pix) (*Upper-left*) and the zoomed regions (100x100 pix). The sensitivity in simulated observations is assumed to be 0.3 of the maximum emission. Here, regions where the signal is less than 0.3 do not show polarization vectors, and $P_{max} = 97\%$.

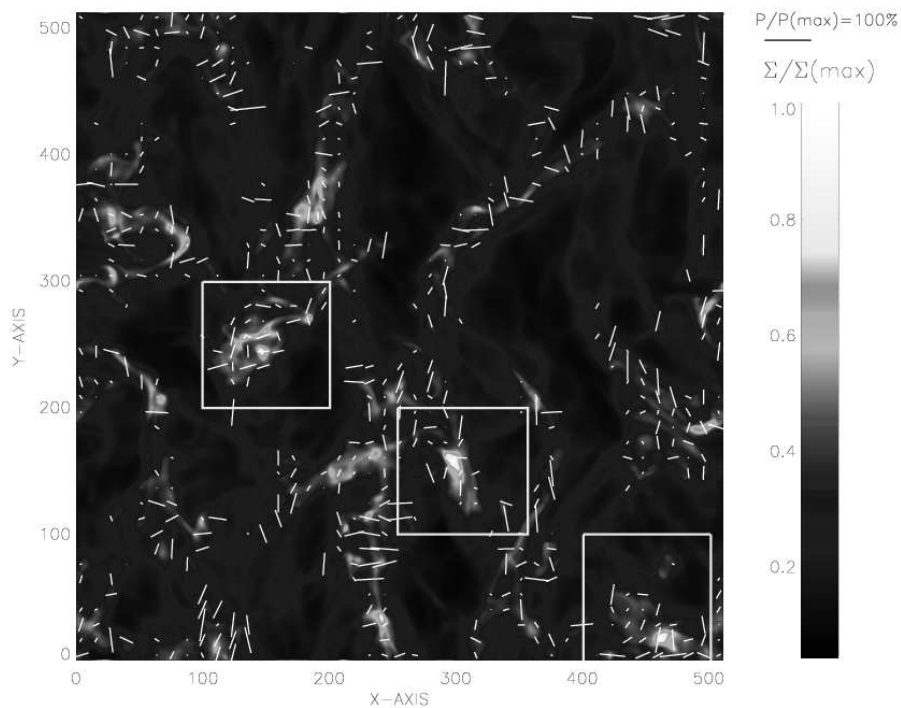


Fig. 2.— Polarization of emission and column density maps for Model 3 ($M_S \sim 7.0$ and $M_A \sim 0.7$) with \mathbf{B}_{ext} parallel to the line of sight. The complete map (512x512 pix) (*Upper-left*) and the zoomed regions (100x100 pix). The sensitivity in simulated observations is assumed to be 0.3 of the maximum emission. Here, regions where the signal is less than 0.3 do not show polarization vectors, and $P_{max} = 85\%$.

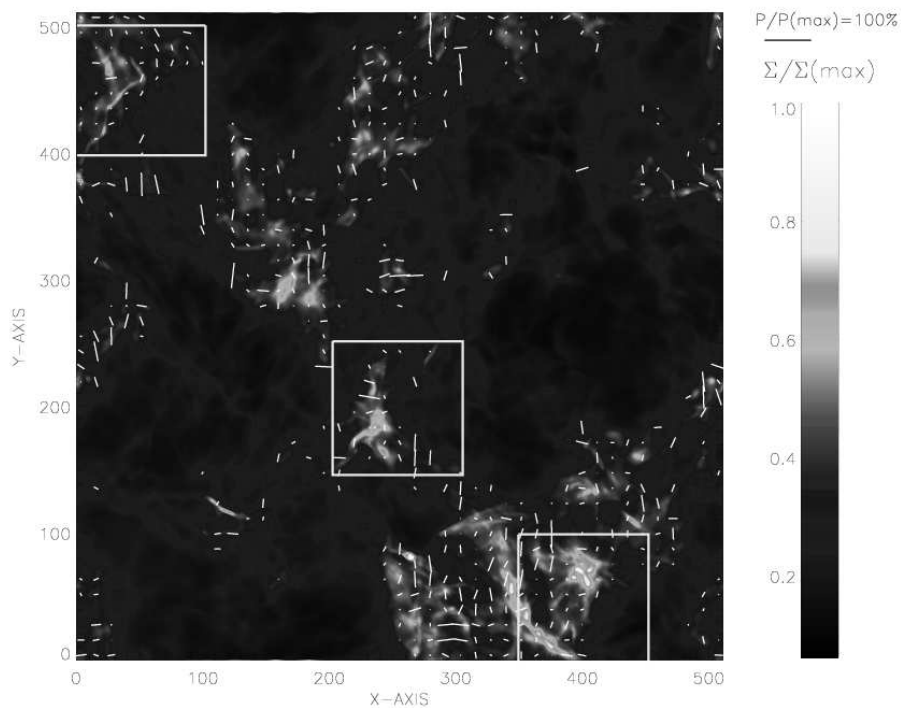


Fig. 3.— Polarization of emission and column density maps for Model 4 ($M_S \sim 7.0$ and $M_A \sim 2.0$) with \mathbf{B}_{ext} perpendicular to the line of sight. The complete map (512x512 pix) (*Upper-left*) and the zoomed regions (100x100 pix). The sensitivity in simulated observations is assumed to be 0.3 of the maximum emission. Regions where the signal is less than 0.3 do not show polarization vectors. Here, regions where the signal is less than 0.3 do not show polarization vectors, and $P_{\max} = 76\%$.

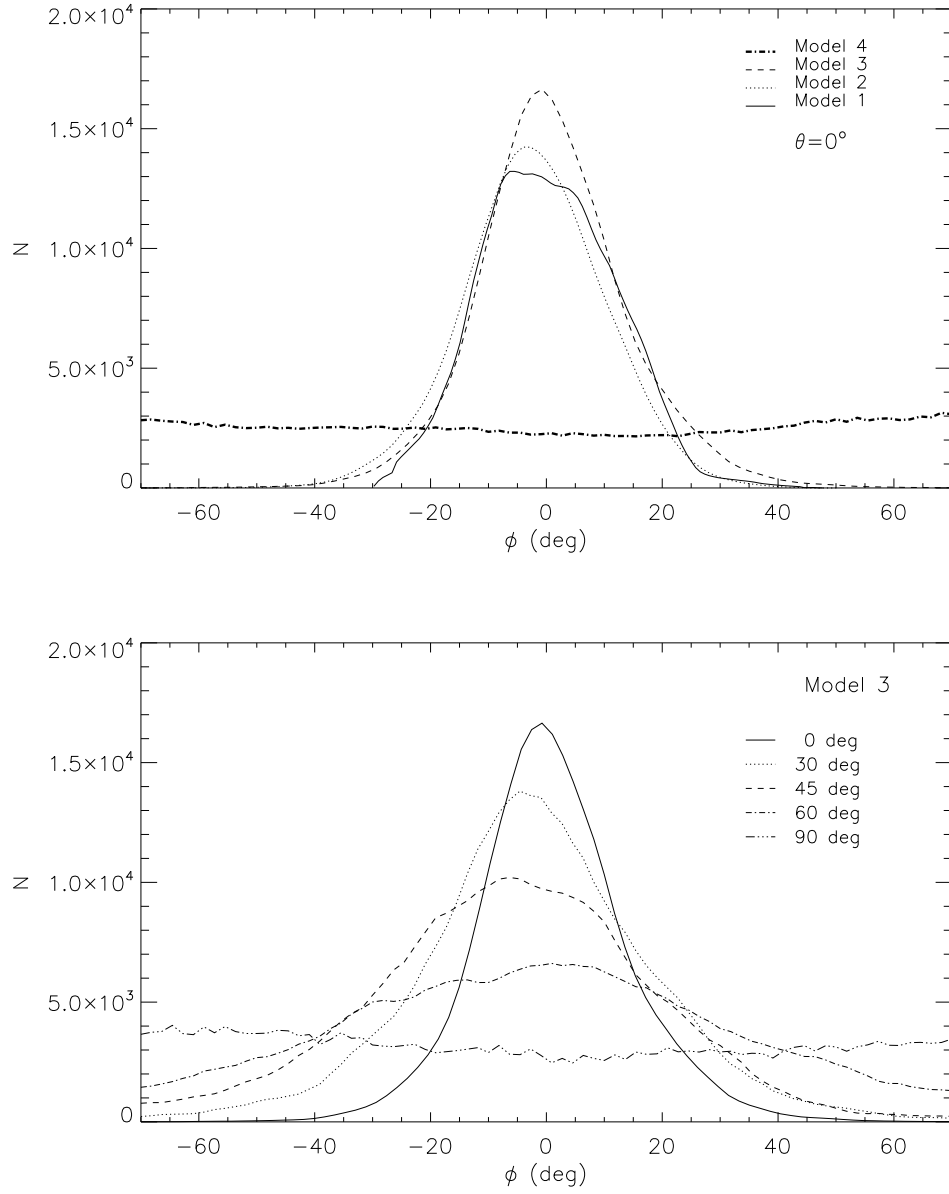


Fig. 4.— Histograms of polarization angle of the different models with $\theta = 0$ (*up*), and for Model 3 and different magnetic field orientations in respect to the line of sight (angles θ) (*bottom*).

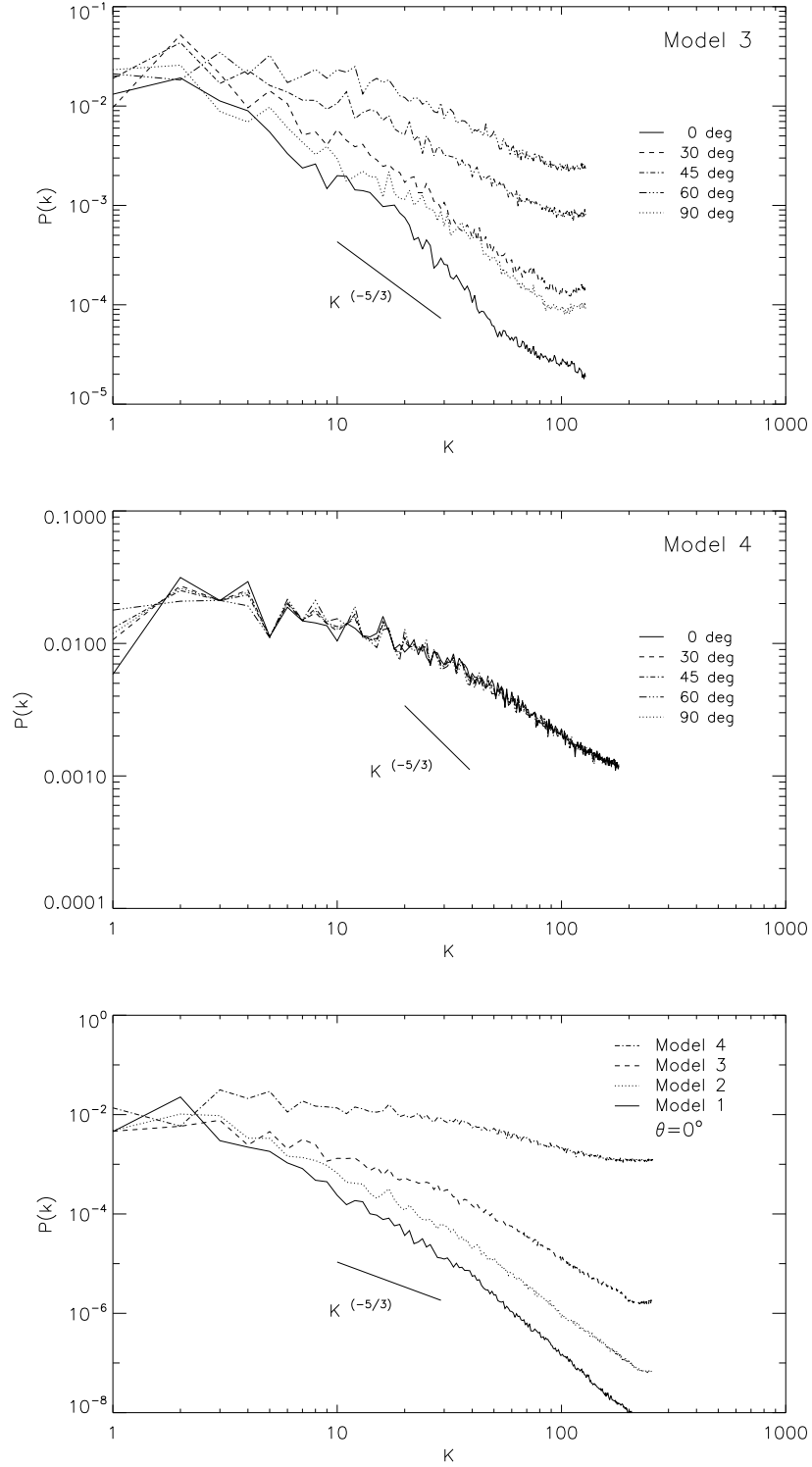


Fig. 5.— Spectra of polarization angle for Model 3 with different magnetic field orientations regarding the line of sight (angles θ) (*up*), Model 4 with different θ (*middle*) and for the different models with magnetic field perpendicular to the line of sight ($\theta = 0$) (*bottom*).

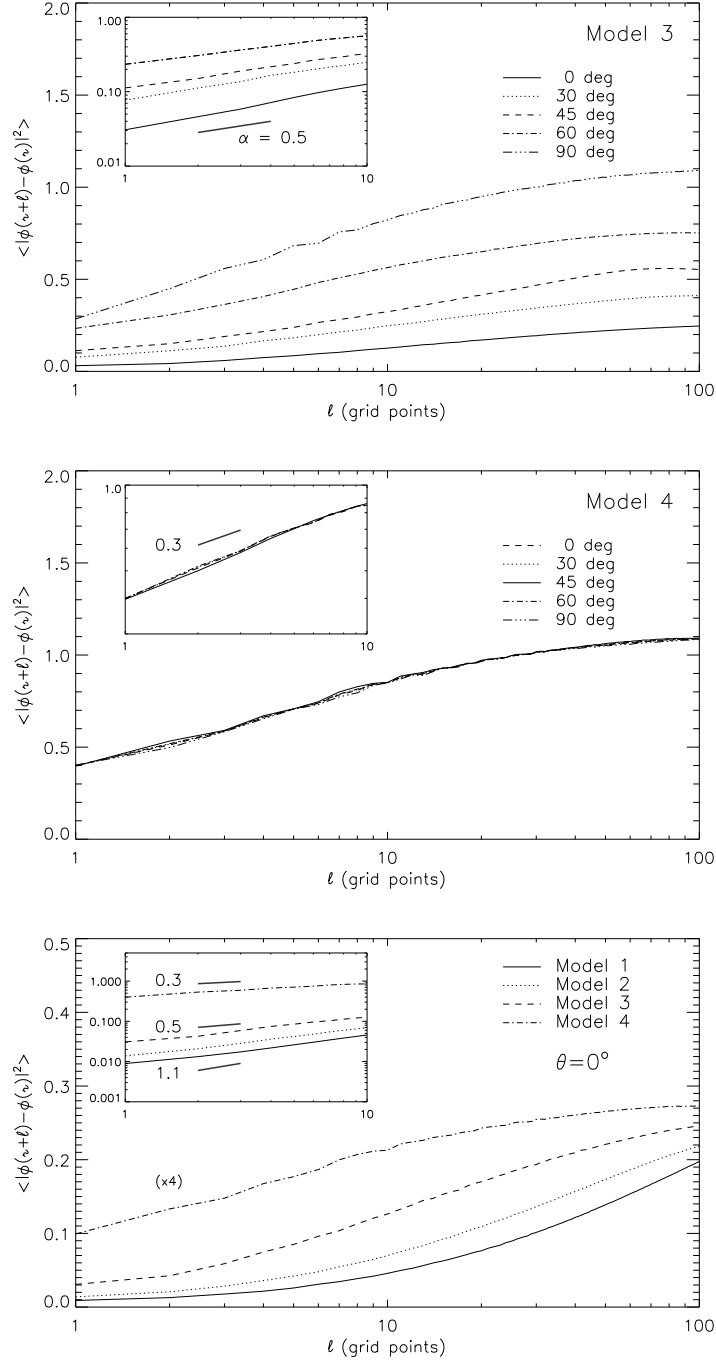


Fig. 6.— Structure functions of polarization angle for Model 3 with different magnetic field orientations regarding the line of sight (angles θ) (*up*), Model 4 with different θ (*middle*) and for the different models with magnetic field perpendicular to the line of sight ($\theta = 0$) (*bottom*).

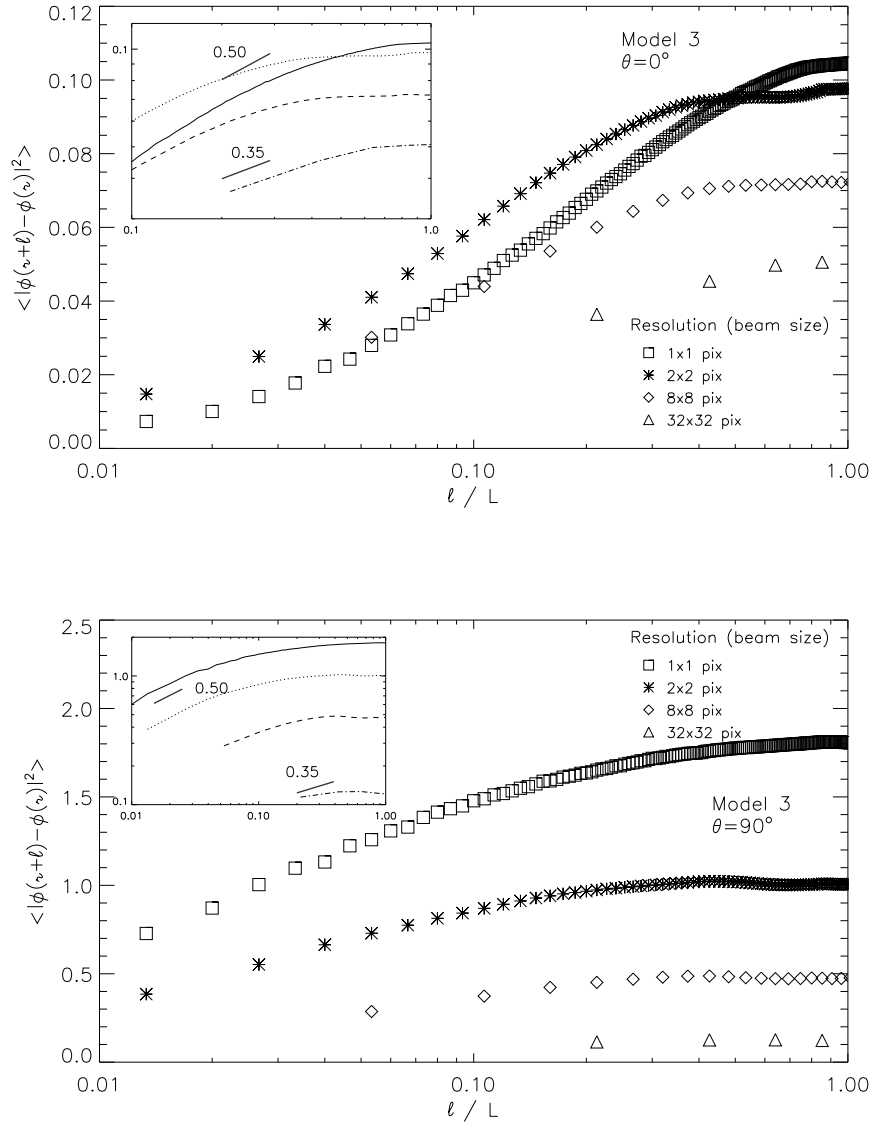


Fig. 7.— Structure functions of polarization angles for Model 3 considering B_{ext} perpendicular (*up*) and parallel to the line of sight (*bottom*).

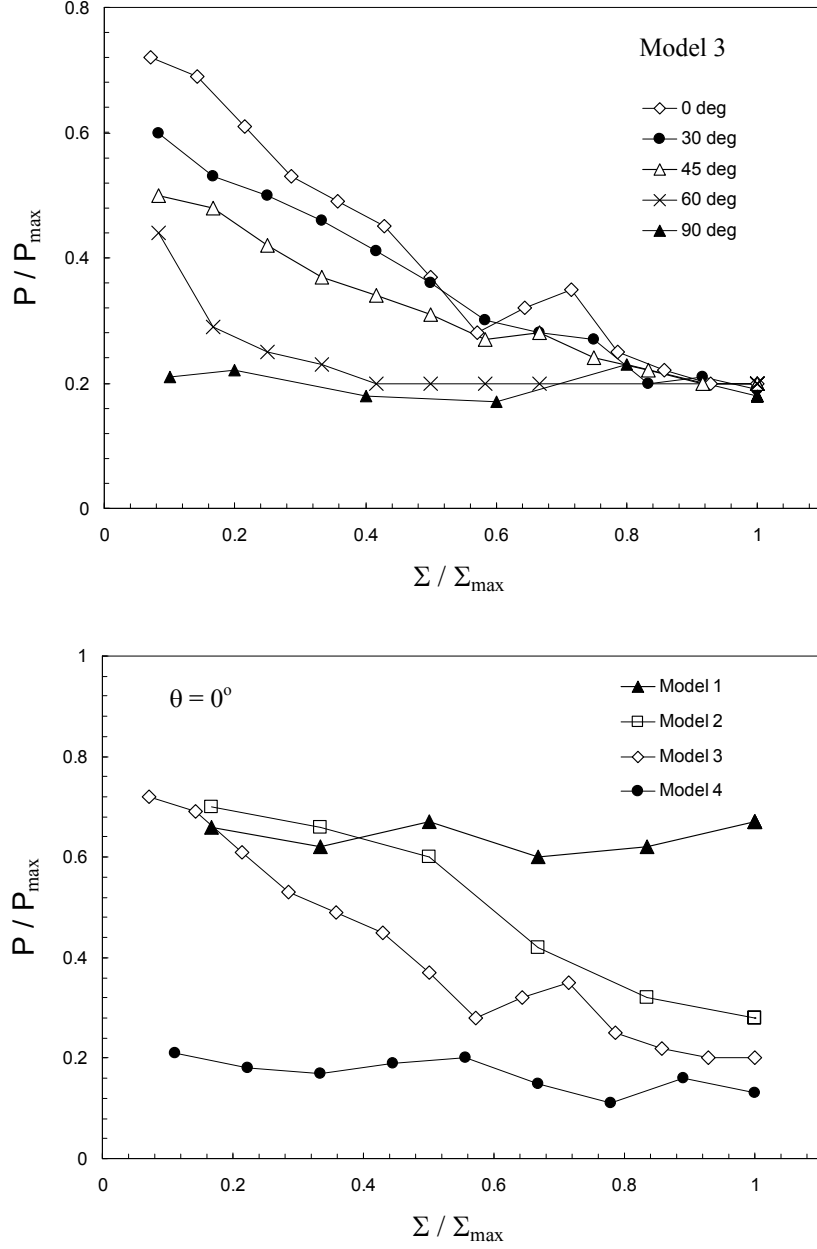


Fig. 8.— Correlation between averaged polarization degree and the column density for Model 3 with different magnetic field orientations regarding the LOS (*up*), and for the different models with $\theta = 0$ (*bottom*). P_{\max} is 100%, 98%, 97% and 85% for Model 1, 2, 3 and 4, respectively.

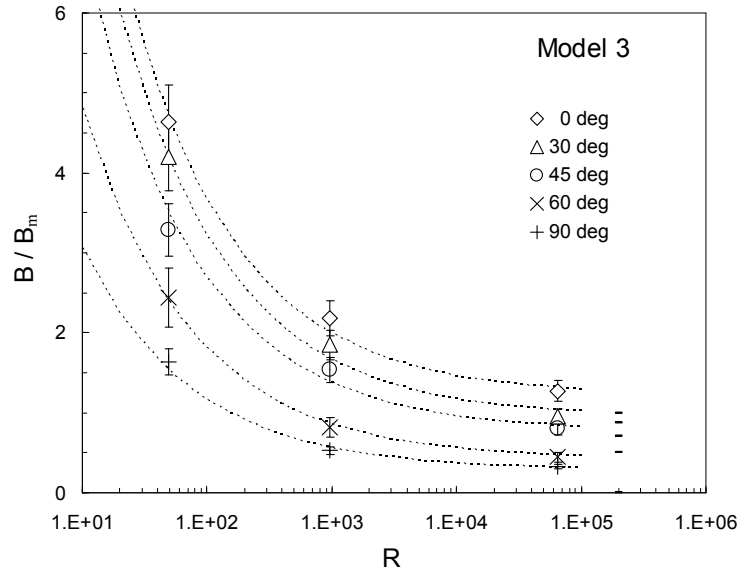


Fig. 9.— CF method calculation for Model 3 with different inclinations with respect to the line of sight. The dotted lines represent the fittings using Eq. (10). The traces indicate the expected value $B^m \cos \theta$.

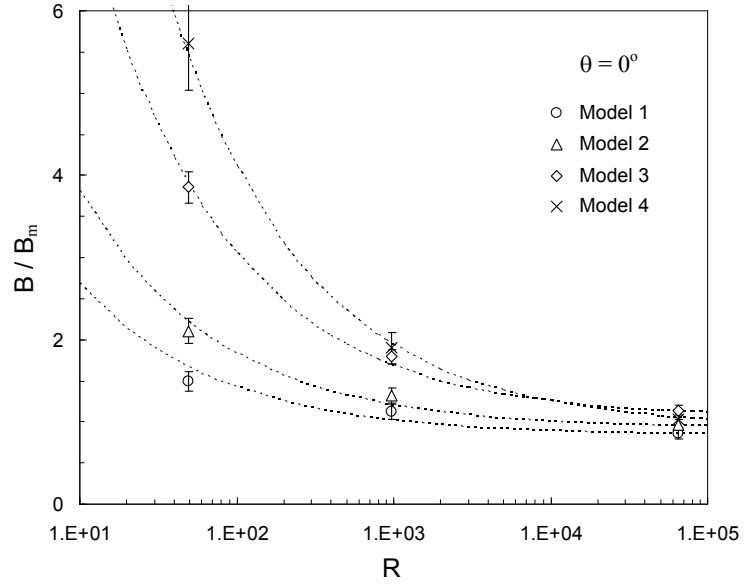


Fig. 10.— CF method calculation for the different models with $\theta = 0$. The dotted lines represent the fittings using Eq. (10).

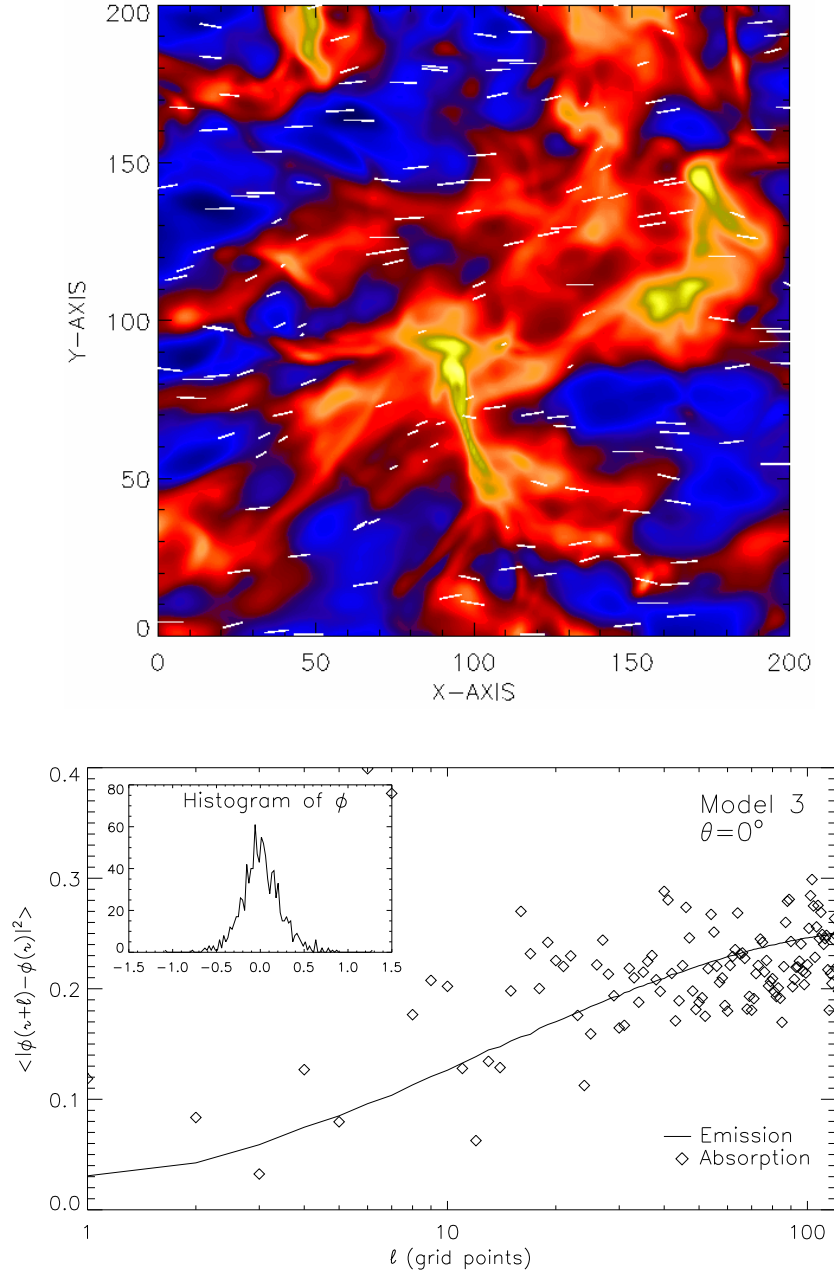


Fig. 11.— Polarization map of absorbed radiation from 1000 randomly positioned background stars. *Up*: column density and polarization vectors of a zoomed region of 200 x 200 pixels for Model 3 with $\theta = 0^\circ$. *Bottom*: histogram of polarization angle for Model 3 with $\theta = 0^\circ$, and its structure function (squares) compared to the emission SF (solid line).